



OPEN ACCESS

EDITED BY

Dunia E. Santiago,
University of Las Palmas de Gran
Canaria, Spain

REVIEWED BY

Sriram Mansingh,
Siksha O Anusandhan University, India
Muthuraj Velluchamy,
Virudhunagar Hindu Nadars'
Senthikumara Nadar College
(Autonomous), India
Ying Cheng,
The University of Newcastle, Australia

*CORRESPONDENCE

Yingxue Sun,
sunyx@th.btbu.edu.cn

SPECIALTY SECTION

This article was submitted to Water and
Wastewater Management,
a section of the journal
Frontiers in Environmental Science

RECEIVED 10 October 2022

ACCEPTED 16 November 2022

PUBLISHED 28 November 2022

CITATION

Liu C, Xie Y, Jiao Y, Du Y, Zheng Q and
Sun Y (2022), Visible-light-driven
nanoscale zero-valent iron loaded rGO/
g-C₃N₄ for fluoroquinolone antibiotics
degradation in water.
Front. Environ. Sci. 10:1065770.
doi: 10.3389/fenvs.2022.1065770

COPYRIGHT

© 2022 Liu, Xie, Jiao, Du, Zheng and
Sun. This is an open-access article
distributed under the terms of the
[Creative Commons Attribution License
\(CC BY\)](https://creativecommons.org/licenses/by/4.0/). The use, distribution or
reproduction in other forums is
permitted, provided the original
author(s) and the copyright owner(s) are
credited and that the original
publication in this journal is cited, in
accordance with accepted academic
practice. No use, distribution or
reproduction is permitted which does
not comply with these terms.

Visible-light-driven nanoscale zero-valent iron loaded rGO/g-C₃N₄ for fluoroquinolone antibiotics degradation in water

Chen Liu¹, Yuqian Xie¹, Yuzhu Jiao^{1,2}, Yongjuan Du^{1,2},
Qinmin Zheng³ and Yingxue Sun^{1,2*}

¹School of Ecology and Environment, Beijing Technology and Business University, Beijing, China, ²State Environmental Protection Key Laboratory of Food Chain Pollution Control, Beijing Technology and Business University, Beijing, China, ³Senseable City Lab, Department of Urban Studies and Planning, Massachusetts Institute of Technology, Cambridge, MA, United States

Fluoroquinolone antibiotics attract increasing attention in the water treatment field because of the potential adverse effects on aquatic ecosystems and human health. The graphitic carbon nitride (g-C₃N₄) based photocatalysis has been demonstrated as an economically feasible and environmentally benign process to control these persistent contaminants. In this study, a new visible-light-driven of reduced graphene oxide (rGO) and nanoscale zero-valent iron (nZVI) co-modified g-C₃N₄-based photocatalyst was synthesized *via* ultrasonication-assisted chemisorption method. The optimized nZVI-loaded rGO/g-C₃N₄ (10% IGCN) showed a reaction rate enhancement of 2.12~3.69-fold and 1.20~1.68-fold for the degradation of ofloxacin (OFL), norfloxacin (NOR), and ciprofloxacin (CIP) compared to that of carbon-doped g-C₃N₄ (MCB_{0.07}) and rGO-supported g-C₃N₄ (7.5% GCN) under the irradiation of simulated visible light, respectively. The enhanced photocatalytic activity can be ascribed to the synergistic effect of nZVI and rGO to improve the separation of charge carriers and boost the harvest of visible light. The degradation mechanisms were explored by scavenger tests and X-ray photoelectron spectroscopy (XPS), indicating that holes (h⁺) played a dominant role in the decomposition of OFL, NOR, and CIP. The piperazine ring and C–N between the piperazine ring and benzene were the primary attack sites of h⁺. In addition, the ring-opening oxidation of benzene (C=C bond) connected by the C–F bond may also be an essential step. This study shed light on the degradation mechanism of OFL, NOR, and CIP under visible light irradiation of the 10% IGCN and provided theoretical support for the practical application of photocatalysis in treating antibiotics-containing water.

KEYWORDS

visible light photocatalysis, modified graphitic carbon nitride, nanoscale zero-valent iron, fluoroquinolone antibiotics, degradation mechanism

1 Introduction

Fluoroquinolones (FQs), one class of broad-spectrum antibiotics widely used in human and veterinary medicine (Zheng et al., 2021; Adeleye et al., 2022), are the most frequently detected antibiotics in aquatic environment considered as a crucial class of emerging pollutants with concentrations ranging from ng/L to $\mu\text{g/L}$ (Lu et al., 2021; Zhou et al., 2021), which not only poses a risk to human health, but also promotes the emergence of antibiotic-resistant bacteria and their resistances (Wallmann et al., 2021; Mangla et al., 2022). In virtue of the stability of quinolone backbone (Zhu et al., 2016), low biodegradability, and high adsorption affinity (Oberoi et al., 2019; Lu et al., 2021; Saya et al., 2022), FQs generally cannot be completely removed by conventional water and wastewater treatment technologies. Therefore, discharge from wastewater treatment plants have become the major pathway for the ubiquity of FQs residues entering in aqueous system. Thus, an innovative, feasible, and environmentally benign process urgently needs to be developed and utilized, and the fate of the FQs requires intensive and further investigations.

Solar-energy-enabled photocatalysis is considered a sustainable process to degrade persistent environmental pollutants *via* the attack of photogenerated reactive species such as holes (h^+) and reactive oxygen species (ROS) ($\bullet\text{OH}$, $^1\text{O}_2$, $\bullet\text{O}_2^-/\bullet\text{HO}_2$, and H_2O_2) (Zheng et al., 2019; Schnabel et al., 2021; Zewdie et al., 2021). Graphitic carbon nitride ($g\text{-C}_3\text{N}_4$) has attained significant attention for the degradation of organic pollutants in water because of its appealing electronic band structure, excellent physicochemical properties, and abundance (Ong et al., 2016; Balakrishnan and Chinthala, 2022). Also, the $g\text{-C}_3\text{N}_4$ photocatalysts can harvest and potentially utilize more sunlight and can be reactive under artificial light, which takes apparent advantages in water purification over conventional photocatalysts (Cui et al., 2021; Lin et al., 2022). However, the photocatalytic activity of original $g\text{-C}_3\text{N}_4$ (e.g., synthesized from melamine) was limited due to the small specific surface area, weak response of visible light, and strong recombination rate of photogenerated electron-hole (e^- - h^+) pairs (Zheng et al., 2017; Nemiwal et al., 2021). Recently, different innovative approaches (e.g., doping, heterojunctions, crystal phase, and facet control) were explored to minimize the drawbacks and enhance the photocatalytic efficiency. Our previous research proved that the C-doped structure could produce ROS under thermodynamically favorable conditions, localize h^+ to improve charge separation, and enhance the photocatalytic degradation of persistent organic micropollutants (Zheng et al., 2017; Chang et al., 2019).

Reduced graphene oxide (rGO), which presents a similar carbon network and sp^2 conjugated π structure with $g\text{-C}_3\text{N}_4$, has attracted considerable attention as an efficient supporter of $g\text{-C}_3\text{N}_4$ to increase the conductivity and accelerate the

separation of photo-generated charge carriers due to π -conjugated built-in electric field in the interface between $g\text{-C}_3\text{N}_4$ and rGO (Saha et al., 2020). Yuan et al. (2019) reported that the photocatalytic degradation efficiency of tetracycline on rGO/ $g\text{-C}_3\text{N}_4$ was more than 80% higher than that of original $g\text{-C}_3\text{N}_4$. Xie et al. (2022) found that a hybrid catalyst of 7.5% rGO/ $g\text{-C}_3\text{N}_4$ presented higher inactivation efficiency on ofloxacin-resistant bacteria under light irradiation. In general, the excellent electron transfer ability of rGO was impregnated to realize the practical separation of photo-generated carriers of $g\text{-C}_3\text{N}_4$. The hybrid catalyst of rGO/ $g\text{-C}_3\text{N}_4$ by related research does show good photocatalytic activity. Consequently, constructing three-phase, composite-based rGO/ $g\text{-C}_3\text{N}_4$ by combining with metals (Au, Ag, Pd, etc.), non-metals (N, B, S, P, F, I, etc.), and other semiconductors (TiO_2 , Bi_2WO_6 , etc.) were explored by many researchers in order to improve further its photocatalytic performance (Kasinathan et al., 2020).

Nanoscale zero-valent iron (nZVI) is also of increasing interest to researchers because of its environmentally harmless, good conductivity, strong reducibility, and high reactivity to organic pollutants (Wang et al., 2020; Wu et al., 2022a). Ma et al. (2021) has synthesized nZVI@ Ti_3C_2 -based MXene nanosheets. The vast majority of ranitidine is found to be degraded with 91.1% of removal efficiency, indicating that nZVI@ Ti_3C_2 -based MXene has a synergistic effect enhancing the catalyst chemical reactivity and stability. Wang et al. (2017) has reported a photocatalyst named $\text{Fe}^0/\text{C}_3\text{N}_4/\text{MoS}_2$ with improved carrier separation efficiency through capturing the photo-generated e^- by nZVI. In addition, although nZVI is easy to be oxidized to $\equiv\text{Fe}^{\text{II}}$ and $\equiv\text{Fe}^{\text{III}}$, it can be reduced to Fe^0 by utilization in photo-generated e^- (Wang et al., 2016; Wang et al., 2019), and further promoting the regeneration and reuse of nZVI. However, several disadvantages of nZVI (easily oxidation, severe aggregation, etc.) has not been effectively resolved. The previous studies have shown that carbon materials can be used as the carrier of nZVI dispersed in the liquid phase, and their application limitations can be remedied through synergistic effects (Fan et al., 2022; Wang et al., 2022).

Therefore, a new efficient strategy to prepare nZVI composites is urgently required. The combination of $g\text{-C}_3\text{N}_4$, rGO, and nZVI will be a potential visible-light-driven photocatalytic technology in accelerating the migration of photo-generated e^- and h^+ and enhancing photocatalytic efficiency. However, there are few reports on the combination of $g\text{-C}_3\text{N}_4$, rGO, and nZVI in the photocatalytic degradation of antibiotic contaminants. Also, because of the selectivity in contaminant degradation of $g\text{-C}_3\text{N}_4$ -based photocatalysts and the resistance to the decomposition of most antibiotics for their robust molecular structures (Zheng et al., 2019; He et al., 2022), designing and fabricating $g\text{-C}_3\text{N}_4$ -based photocatalysts with high activities requires further research.

Herein, in the present work, the modification of $g\text{-C}_3\text{N}_4$ by rGO and nZVI was realized *via* ultrasonication-assisted

chemisorption. The nZVI-loaded rGO/g-C₃N₄ was characterized and the photodegradation of ofloxacin (OFL), norfloxacin (NOR), and ciprofloxacin (CIP) by nZVI-loaded rGO/g-C₃N₄ were evaluated by scavenger-quenching experiment. The main photo-generated reactive species involved in the degradation of OFL, NOR, and CIP were explored by scavenger-quenching experiments. And the X-ray photoelectron spectroscopy (XPS) was used to study the changes of the surface characteristic groups of nZVI-loaded rGO/g-C₃N₄ before and after photocatalysis, and speculated the degradation mechanism and possible pathway. Meanwhile, the stability of nZVI-loaded rGO/g-C₃N₄ was evaluated through cycle experiment. This study will open a new horizon in the modification of g-C₃N₄ and provide a feasible treatment technology to remove FQs pollutants from water.

2 Materials and methods

2.1 Modified preparation of g-C₃N₄ photocatalysts

To improve the separation efficiency of photo-generated charge carriers, we first introduce the rGO onto substrate g-C₃N₄ to form n% GCN composite. After the optimization of rGO introduction on the substrate g-C₃N₄, the electron mediator nZVI was then introduced to form n% IGCN composite.

The substrate g-C₃N₄, which is named MCB_{0.07}, was prepared by melamine (2 g), cyanuric acid (1.93 g), and barbituric acid (0.07 g) according to our previous study (Zheng et al., 2016). Then, the rGO was introduced on the basis of MCB_{0.07} (n% GCN, n stood for the mass ratio of graphene oxide (GO) to melamine). Melamine (2 g), cyanuric acid (1.93 g), barbituric acid (0.07 g) and a certain volume of GO dispersion liquid were added into the anhydrous ethanol of 40 ml. The powder was first stirred for 3 h (500 r/min) at 25°C, then ultrasonic treatment for 3 h, and finally dried in 70°C oven to obtain gray-white powder without liquid. The gray-white powder was then transferred into a covered alumina crucible and calcined in a muffle furnace at 550°C for 4 h with a heating rate of 2.3°C/min. After natural cooling, the obtained solid is grounded into powder, which was denoted as n% GCN. In order to prove that GO was thermally reduced to rGO at high temperatures, the GO dispersion was dried in an oven at 70°C, and heated in a muffle furnace at 550°C for 4 h with a heating rate of 2.3°C/min.

The nZVI modification was introduced on the basis of 7.5% GCN (n% IGCN, n was the mass ratio of nZVI and n% GCN) by a facile ultrasonication-assisted chemisorption method. All n% IGCN samples were freshly prepared to prevent the oxidation of nZVI. Specifically, a certain amount of 7.5% GCN and nZVI were dispersed in 10 ml of ultrapure water (ultrapure water was under

N₂ gas flow in advance) to prepare n% IGCN stock solution. Before the photocatalytic experiment, the n% IGCN stock solution was ultrasonicated for 1 min (KQ-300DE, 60 kHz) to achieve a uniform suspension. The synthesized schematic of the n% IGCN photocatalyst is shown in Figure 1.

2.2 Characterization

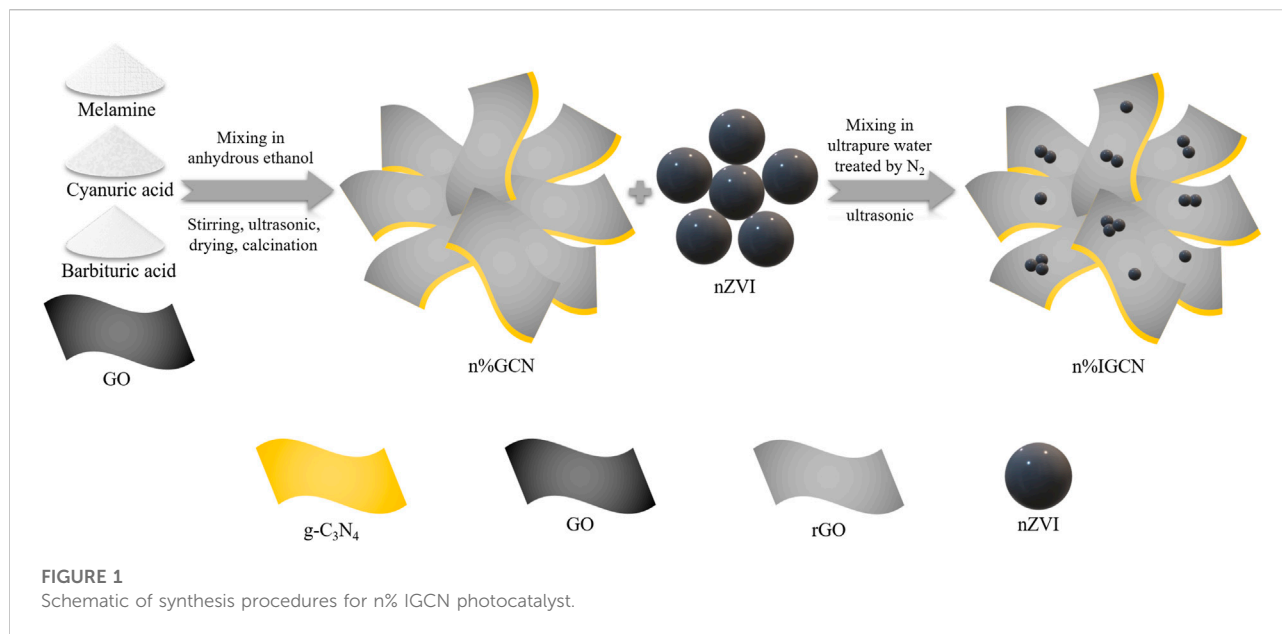
The surface micro-morphology of samples was detected by field emission scanning electron microscopy (FE-SEM, Sigma 300, Germany) equipped with energy dispersive X-ray spectroscopy (EDS), and transmission electron microscopy (TEM, JEM-2100, Japan). The specific surface area of the samples was determined at 77 K using a gas adsorption instrument (NOVA-2000e, United States) after vacuum degassing under 300°C for 12 h, then pore structure was calculated. The crystal structures of samples were investigated using an X-ray diffractometer (XRD, Rigaku Dmax-2500, Japan) with Cu-K α radiation ($\lambda = 1.5406 \text{ \AA}$) in the scanning range of $2\theta = 5\text{--}90^\circ$. Fourier transform infrared spectroscopy (FTIR, Nicolet iS5, United States) measurement was carried out to characterize the functional groups in the 400–4,000 cm⁻¹ range, and prepare KBr for use as a blank control group.

The valences and existing forms of the elements on the samples were analyzed using X-ray photoelectron spectroscopy (XPS, EscaLab Xi+, United States) with monochromated Al-K α radiation ($h\nu = 1,486.6 \text{ eV}$) as the excitation source, and the binding energy values were calibrated concerning C1s = 284.80 eV. All the binding energies of functional groups were determined according to the NIST XPS Database. All materials were vacuum freeze-drying for 24 h to remove the interference of residual H₂O and prevent the oxidation of some components. The diffuse reflectance spectroscopy (DRS, UV-3600, Japan) was used to further evaluate the optical properties of the catalysts with BaSO₄ as the background level. The detailed calculation method of band gap (E_g) was given in Supplementary Text S1.

Photoluminescence (PL, FLS-980, GBR) spectra were obtained with an excitation wavelength of 345 nm and an emission range between 400 and 650 nm to determine the transport characteristics of charge carriers. The transient photocurrent responses and electrochemical impedance spectroscopy (EIS) were measured with an electrochemical analyzer (CS310H, China). The measurement method was given in Supplementary Text S2.

2.3 Photocatalytic experiments

Photocatalytic degradation experiments were conducted in a photochemical reaction apparatus (66924-1000HX-R1, Newport, United States) with direct research grade arc lamp



source equipped with an ozone-free xenon lamp (1000 W) (6295NS, Newport, United States), liquid filter (6213NS, Newport, United States), and a 400 nm filter to filter infrared and UV light out. The reaction temperature was maintained at $25 \pm 0.2^\circ\text{C}$ by a circulating water system. The distance between the light source and the liquid surface was 13.5 cm. The intensity of light with a wavelength greater than 400 nm ($\lambda > 400 \text{ nm}$) was 220.3 mW/cm^2 . The photocatalytic reaction was carried out in a 300 ml jacket beaker. The initial concentration of phenol or different antibiotics (OFL, NOR, and CIP) was 10 mg/L, and the pH was maintained at 7.0 by adding phosphate buffer solution (PBS). The photocatalyst loading was 1 g/L, and the solution was magnetically stirred at 500 r/min. The solution and photocatalyst were mixed at dark for 20 min to reach adsorption-desorption equilibrium before the photocatalytic reaction. During the photocatalytic reaction under light irradiation, a certain amount of liquid sample was collected at regular time intervals and stored in a 4°C refrigerator after passing through a $0.22 \mu\text{m}$ filter membrane for further analysis.

2.4 Scavenger-quenching experiments

Scavenger tests were employed by quenching selected reactive species generated in the photocatalytic system to study the contribution of a specific reactive species to the degradation of pollutants. The isopropyl alcohol (IPA), L-histidine (L-His), p-Benzoquinone (BQ), catalase, and ethylenediaminetetraacetic acid disodium salt dihydrate (EDTA-2Na) were used to quench the $\bullet\text{OH}$, $^1\text{O}_2$, $\bullet\text{O}_2^-$, H_2O_2 ,

and h^+ , respectively. The concentration of IPA, L-His, and catalase was 0.1 mol/L, 10 mmol/L, and 1,000 U/mL, respectively. The concentrations of BQ and EDTA-2Na were 4 mmol/L, respectively. The inhibition rate of the scavenger to the reaction is shown in Eq. 1:

$$R = \frac{N_0 - N_a}{N_0} \quad (1)$$

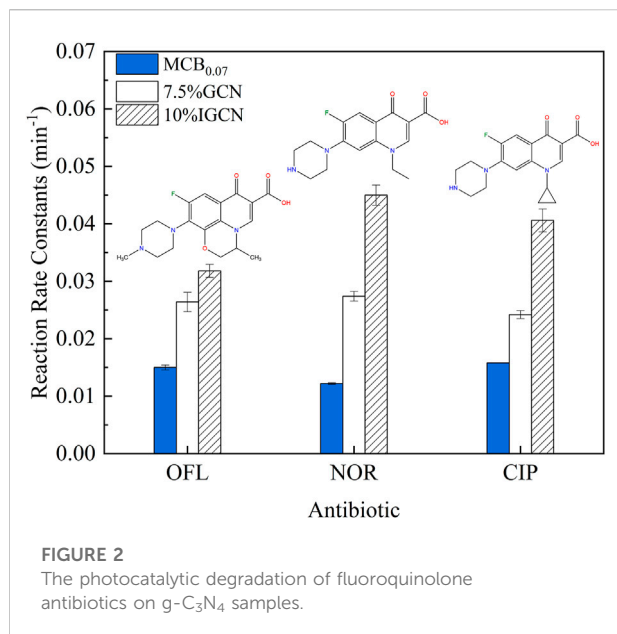
Where N_0 , N_a is the degradation percentage of pollutants with and without adding scavenger, respectively.

2.5 Analytical methods

The concentration of phenol was determined by 4-aminoantipyrine spectrophotometry (HJ503-2009). The dissolved organic carbon (DOC) of the solution was determined by total organic carbon analyzer (Vario TOC, Germany). The temperature, pressure, and flow rate of the combustion tube were set at $850 \pm 1^\circ\text{C}$, $1,000 \pm 30 \text{ Pa}$, and $180 \pm 5 \text{ ml/min}$, respectively. The water sample was tested after passing through a $0.22 \mu\text{m}$ membrane.

The concentrations of OFL, NOR, and CIP were analyzed using high performance liquid chromatography (HPLC, 1,260 Infinity II, United States) equipped with Venusil MP C18 reversed-phase chromatographic column ($4.6 \text{ mm} \times 250 \text{ mm} \times 5 \mu\text{m}$). The specific HPLC analysis method of OFL, NOR, and CIP were summarized in [Supplementary Table S1](#).

The fluoride ion concentration was detected by ion chromatography (IC, Dionex ICS-1100, United States) equipped with AS23 ($4 \text{ nm} \times 250 \text{ nm}$) column.



2.6 Cycling run experiments

The regenerated photocatalysts were collected by using a 0.22 μm membrane, washed with ultrapure water for several times with ultrasonication, and dried at 105°C for 24 h. The regenerated photocatalysts were then used to degrade OFL, NOR, and CIP for multiple cycles as described in Section 2.3.

3 Results and discussion

3.1 Comparison of photocatalysts

The loading of rGO and nZVI was optimized using phenol degradation kinetics as a performance indicator. 0%–10% rGO was introduced for the synthesis of n% GCN, and then 0%–15% nZVI was applied for the synthesis of n% IGCN. The degradation of phenol on various composites is shown in Supplementary Figures S1, S2 and Supplementary Tables S2, S3. It showed that 7.5% GCN and 10% IGCN had the highest degradation effects on phenol under the visible light ($\lambda > 400$ nm), which were 79.7% and 86%. Compared to the 72.7% degradation of phenol by MCB_{0.07}, the removal efficiency of n% GCN and n% IGCN has been effectively improved.

The photocatalytic degradation of OFL, NOR, and CIP on MCB_{0.07}, 7.5% GCN, and 10% IGCN are shown in Figure 2. Under visible light ($\lambda > 400$ nm) irradiation, the degradation of the antibiotic conformed well to the first-order kinetics. The reaction rate constants of MCB_{0.07}, 7.5% GCN, and 10% IGCN were 0.0150 min⁻¹, 0.0264 min⁻¹, and 0.0318 min⁻¹ for the degradation of OFL, 0.0122 min⁻¹, 0.0274 min⁻¹, and

0.0450 min⁻¹ for the degradation of NOR, and 0.0158 min⁻¹, 0.0242 min⁻¹, and 0.0406 min⁻¹ for the degradation of CIP, respectively. The degradation rate of 10% IGCN for the three antibiotics was the highest, indicating that the loading of rGO and nZVI can effectively improve the photocatalytic activity of g-C₃N₄. As shown in Supplementary Figure S3, the oxidation of OFL, NOR, and CIP is not complete, which indicates the existence of oxidation intermediates. The photolysis of OFL, NOR, and CIP under visible light irradiation, shown in Supplementary Table S4, are 8.28%, 8.10%, and 9.64%, respectively, which show the little effect on the photocatalytic degradation process.

The adsorption of OFL, NOR, and CIP on synthesized photocatalysts was evaluated under dark conditions. As shown in Supplementary Figure S4, it was found that the adsorption capacity of three quinolone antibiotics for the same photocatalytic material is not much different, but the adsorption capacity of different photocatalytic materials for the three quinolone antibiotics is obviously different. The removal efficiencies of OFL, NOR, and CIP were 14.63%, 14.24%, and 15.90% using MCB_{0.07}, respectively. Moreover, the removal efficiencies of OFL, NOR, and CIP were 5.88%, 6.91%, and 6.60% using 10% IGCN, respectively. The decreasing adsorption capacity of MCB_{0.07}, 7.5% GCN and 10% IGCN for fluoroquinolone antibiotics is related to the reduction of active sites due to the loading of rGO and nZVI as shown by the decrease of BET surface area (Supplementary Figure S5) and pore volume (Supplementary Figure S6). The adsorption of OFL, NOR, and CIP on each photocatalyst was comparable and the photocatalytic experiments were conducted after the adsorption reaching the equilibrium. Therefore, the adsorption effect was neglectable to photocatalytic degradation. Secondly, MCB_{0.07} has the highest static adsorption rate, but its ability that produces reactive oxygen species is relatively poor. While 10% IGCN has a weak adsorption capacity, it has a solid ability to produce reactive oxygen species (the removal effect of 10% IGCN for three antibiotics was seen in Section 3.3). Therefore, the strong adsorption capacity is not necessarily related to the high organic matter removal capacity.

3.2 Characterization of photocatalysts

To observe the morphological and microstructural features of as-prepared samples, scanning electron microscopy (SEM) and transmission electron microscopy (TEM) images were investigated. As shown in Figure 3A, the MCB_{0.07} showed an abundant porous structure distributing evenly and densely on the surface, which was consistent with previous studies (Zheng et al., 2016; Chang et al., 2019). The original GO exhibits an irregular layered flaky structure with rough edges and smooth surfaces, shown in Figure 3D (Liu et al., 2017). According to the previous work, after 550°C treatment, GO was reduced to rGO (Shanavas

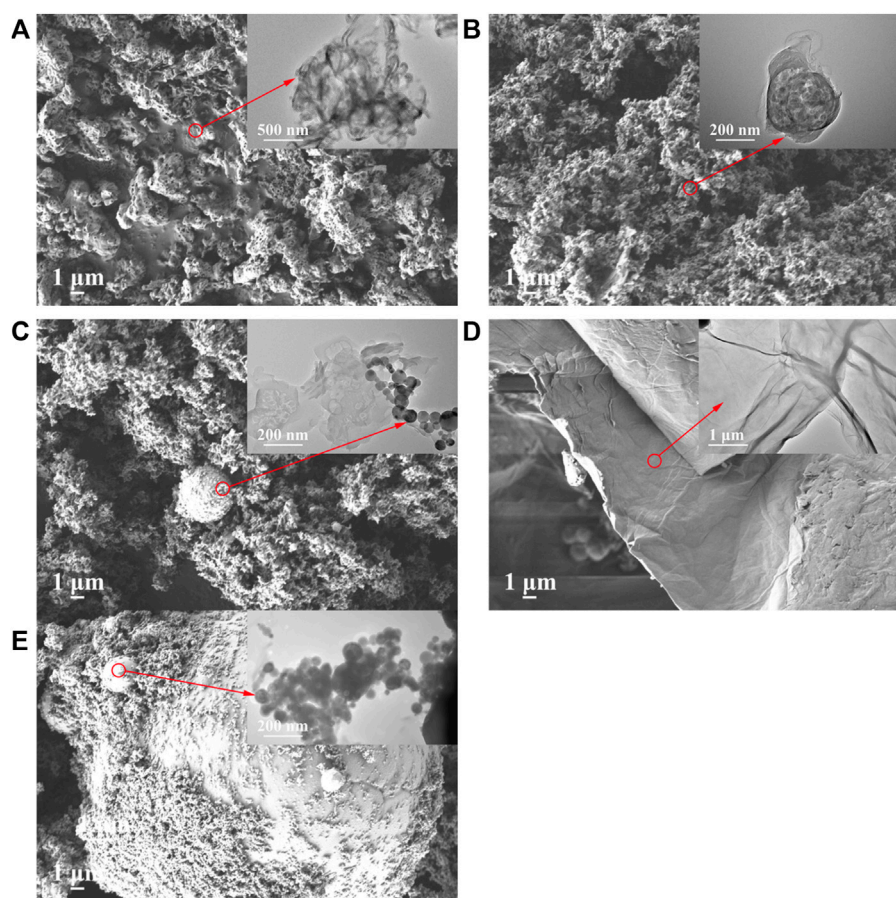


FIGURE 3

SEM and TEM of g-C₃N₄ series modified samples (A) MCB_{0.07}, (B) 7.5% GCN, (C) 10% IGCN, (D) GO and (E) nZVI (the corresponding TEM image in the upper right corner).

et al., 2019; Hu et al., 2021), while the wrinkles and curls could be observed from rGO (Agarwal and Zetterlund, 2021). However, although the porous structure of 7.5% GCN and the interface between rGO and MCB_{0.07} can be observed (Figure 3B), the pore of 7.5% GCN was inapparent and messy than MCB_{0.07}. This may be due to the introduction of rGO layers, which upset the pore structure of MCB. This was consistent with the Brunauer-Emmett-Teller (BET) results. The pristine nZVI particles exhibit uncontrollable agglomeration, shown in Figure 3E. After loading nZVI on 7.5% GCN to synthesize 10% IGCN, it was observed that nZVI spherical particles were successfully attached to the sheet layer of 7.5% GCN with slight agglomeration (Figure 3C).

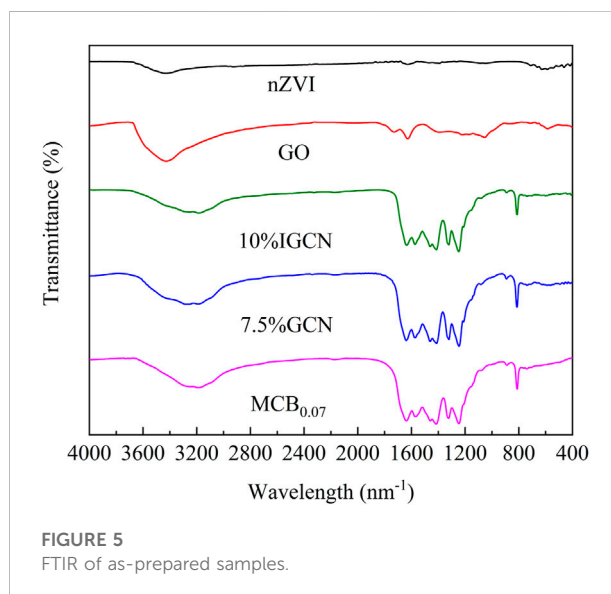
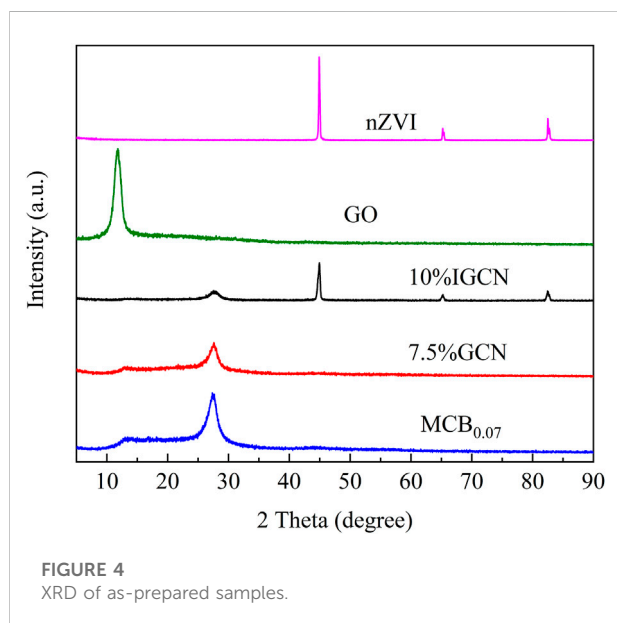
The energy dispersive X-ray spectroscopy (EDS) of MCB_{0.07}, 7.5% GCN, and 10% IGCN composites showed that C and N were uniformly distributed, and O was also presented due to incomplete polymerization of cyanuric acid or barbituric acid on g-C₃N₄ and the residual O-containing functional groups of rGO (Supplementary Figures S7, S8). As shown in Supplementary

Table S5, the weight ratio of C and O in 7.5% GCN and 10% IGCN increased, while the weight ratio of N decreased compared with MCB_{0.07}. This can indicate that rGO was successfully introduced to the sample since rGO has residual O-containing groups (Hu et al., 2021). The presence of about 2.52% Fe on 10% IGCN indicated the successful loading of nZVI, and Fe was also uniformly distributed on the samples.

The pore structures and BET specific surface area of the as-synthesized samples were further characterized by the N₂ adsorption-desorption isotherm method. As shown in Supplementary Figure S5, MCB_{0.07}, 7.5% GCN, and 10% IGCN all presented a representative type-IV curve with a high adsorption capacity at high relative pressures, indicating that they all have the highly porous structure (Li et al., 2015). In addition, mesopores were the main pore structure of three photocatalysts (Supplementary Figure S6; Table 1). However, the BET surface area and total pore volume of MCB_{0.07}, 7.5% GCN, and 10% IGCN showed a decreasing trend. MCB_{0.07} showed the highest BET surface area (104.139 m²/g) and pore

TABLE 1 The specific surface area and pore structure of synthesized samples.

Samples	Total pore volumes (cm ³ /g)	Average pore diameters (nm)	Specific surface area (m ² /g)	Mesopore volumes (cm ³ /g)
MCB _{0.07}	0.270	10.354	104.139	0.249
7.5% GCN	0.225	11.305	79.558	0.214
10% IGCN	0.163	12.108	53.739	0.155
GO	0.452	9.931	181.991	0.410
nZVI	0.00608	3.870	6.280	0.006



volume (0.270 cm³/g). Although the BET surface area of GO was determined to be 181.991 m²/g, the BET surface area and total pore volume of 7.5% GCN dropped to 79.558 m²/g and 0.225 cm³/g, respectively. This may be explained by the fact that the pores of MCB_{0.07} were destroyed by the rGO lamellar texture (Shao et al., 2016). With further loading of nZVI, nZVI may block the part of the pores on 10% IGCN as a result of the smaller size of nZVI particles (Rao et al., 2021), the BET surface area and total pore volume of 10% IGCN further decreased to 53.739 m²/g and 0.163 cm³/g, respectively. However, the removal efficiency of OFL, NOR, and CIP on 10% IGCN was higher than the other two photocatalysts (Figure 2), which indicated that the enhanced photocatalytic activity of the samples has no direct relationship with the BET surface areas, even though the parts of reactive sites of g-C₃N₄ were sacrificed due to the modification of nZVI and rGO.

The crystal structures of the as-prepared samples are determined by X-ray diffraction (XRD), shown in Figure 4. Two distinct and typical diffraction peaks at 13.0° and 27.34° (ICDD No. 87–1,526) were observed for MCB_{0.07}, 7.5% GCN,

and 10% IGCN, which are indexed to g-C₃N₄. The stronger peak at 27.34° was assigned to (002) crystal plane originating from the interlayer-stacking structure of a conjugated aromatic system (Liu et al., 2019), while the weaker peak at 13.0° corresponded to the (001) crystal plane originated from in-plane structural packing motif of tri-s-triazine units (Chang et al., 2019), respectively. However, the characteristic peaks of 7.5% GCN and 10% IGCN exhibited a slight shift compared with MCB_{0.07}, which was attributed to the lattice strain generated in the hybridization process of MCB_{0.07} and rGO (Chen et al., 2020b). The GO sample presented a strong diffraction peak at 10.8° corresponding to the (001) crystal plane (Feng et al., 2022). Nevertheless, a new diffraction peak at 25.2° is detected after the GO treated under 550°C, shown in Supplementary Figure S9, being in accord with (002) crystal plane (Jaiswal et al., 2020), which provided the evidence for the conclusion that the GO was thermally reduced to rGO. However, the diffraction peaks of rGO were not detected in 7.5% GCN and 10% IGCN. It may be due to the content of rGO being too low to be detected (Tang et al., 2022). After nZVI loaded on 7.5% GCN, three typical diffraction peaks at 44.94°, 65.26°, and 82.46° were observed in the image of

10% IGCN, corresponding to (110), (200), and (211) crystal planes (ICDD No. 87–0722) (Huang et al., 2020), respectively. This indicated that the nZVI was successfully loaded without apparent oxidation, which may be credited with the protective effect of graphene materials on nZVI (Wang et al., 2019).

The molecular structures of the as-prepared samples were further examined by Fourier-transform infrared (FTIR) spectroscopy. As shown in Figure 5, the MCB_{0.07}, 7.5% GCN, and 10% IGCN showed the typical absorption peaks with g-C₃N₄. The broad peaks between 2,850 and 3,600 cm⁻¹ were from the stretching vibration of O–H bands and N–H components (Wang et al., 2019; Xiao et al., 2021). This indicated that the presence of unpolymerized–NH₂/=NH groups at the defect sites of the aromatic ring in the cyclic g-C₃N₄ structure was identified (Shanavas et al., 2019). Besides, according to the study of (Huang et al., 2021), the incomplete polymerized fragments of g-C₃N₄ play a leading role in the separation of charge carriers. In addition, the peaks at 1,200–1,650 cm⁻¹ can be attributed to the skeletal stretching vibration modes of a heptazine heterocyclic ring (Li et al., 2015) containing the N–(C)3 or bridging C–NH–C units (Kim et al., 2020). The sharp peak at 812 cm⁻¹ was the breathing mode of the tri-s-triazine ring (Xiao et al., 2021). Compared with the GO sample, the characteristic peaks of GO were not detected in the 7.5% GCN and 10% IGCN samples. This may be explained by the carboxyl, carbonyl, and ester bonds on the surface of GO were reduced at 550°C to form rGO. In addition, as a result of the small amount of rGO in 7.5% GCN and 10% IGCN, the typical peaks were not obvious or merged with the peaks of g-C₃N₄. That was mutually supportive of the XRD results.

The compositions and chemical states of 10% IGCN were analyzed by X-ray photoelectron spectroscopy (XPS). As shown in Supplementary Figure S10, 10% IGCN was mainly composed of C, N, O, and Fe. For a closer examination of C, N, O, and Fe peaks, high-resolution XPS scans over C 1s, N 1s, O 1s, and Fe 2p of 10% IGCN sample were obtained, respectively. The high-resolution XPS scans over C 1s of 10% IGCN contained three components located at 284.8, 286.4, and 288.4 eV. The peak at 284.8 eV is assigned to the alkyl carbon (C–C) (Zhou et al., 2018), which may be proof of the interaction between rGO and g-C₃N₄ (Palanivel et al., 2021). The peak of 286.4 and 288.4 eV are assigned to the C–O bonds (Wu et al., 2022b) and sp² carbon (N–C=N) presented in the framework of g-C₃N₄ (Zhou et al., 2018), respectively, as shown in Supplementary Figure S11A. As shown in Supplementary Figure S11B, the high-resolution scans over N 1s peaks could be deconvoluted into three peaks with binding energies of 399, 400.3, and 401.4 eV, corresponding to the aromatic N with sp²-hybridization bonded with C (C–N=C) (Shanavas et al., 2019; Zeng et al., 2020), the N–(C)3 groups at the edges of heptazine units (Xiao et al., 2021), and the amino functions (C–NH) which are derived from the terminal amino groups on the surface (Zhou et al., 2018), respectively. As shown in Supplementary Figure S11C, the high-resolution XPS scans

over O 1s of 10% IGCN showed that three typical peaks were found with binding energies located at 529.9, 531.5, and 532.9 eV, respectively. The peak at 529.9 eV attributes to the Fe–O bond (Wang et al., 2021b) because of the partial oxidation of nZVI. In addition, the peaks located at 531.5 and 532.9 eV are associated with the C=O bond and organic C–O bond (Chen et al., 2021) due to incomplete polymerization of cyanuric acid or barbituric acid. Most notably, according to the previous research (Xie et al., 2022), compared with 7.5% GCN, the binding energies of C 1s, N 1s, and O 1s of 10% IGCN exhibited a distinct increase, which revealed that an intense interaction could be found between nZVI and 7.5% GCN rather than a simple physical mixing. The Fe species that existed in 10% IGCN were composed of Fe⁰ and oxidation states (e.g., Fe²⁺ and Fe³⁺) (Supplementary Figures S11C,D). The peaks at 707.2 and 720.4 eV of Fe 2p high-resolution XPS scans corresponded to Fe⁰ 2p_{3/2} and Fe 2p_{1/2} (Lv et al., 2021), respectively. It indicated that nZVI was loaded successfully. The presence of Fe³⁺ and Fe²⁺ was shown by the peaks of Fe 2p_{3/2} and Fe 2p_{1/2} at 711.9 and 725.9 eV and 710.6 and 724.3 eV (Ma et al., 2021), which represented that only a small amount of nZVI was inevitably oxidized on the particle surface in the preparation of 10% IGCN because of the high activity of nZVI (Liang et al., 2016; Kong et al., 2021; Rao et al., 2021).

The optical absorption properties of as-synthesized photocatalysts were characterized by measuring the UV-vis diffuse reflectance spectrum (UV-Vis DRS). The spectra (Supplementary Figure S12) indicate that the visible light absorption of MCB_{0.07} is greatly enhanced *via* rGO and nZVI modification. Notably, the absorption edges of MCB_{0.07}, 7.5% GCN, and 10% IGCN were found to be 460 nm, 468 nm, and 599 nm, corresponding to the band gaps (E_g) of 2.70 eV, 2.65 eV, and 2.07 eV, respectively, which represented that the capability of harvesting and utilizing visible light photons were enhanced obviously. Compared to MCB_{0.07}, a slightly red shift was observed in 7.5% GCN, which may attribute to the intrinsic absorption of black-colored rGO (Shao et al., 2016) and the enhancement of π–π* conjugation effect by rGO is indispensable for the change (Tang et al., 2022). With further loading of the nZVI, 10% IGCN showed an intensive absorption in visible light region. This is probably relevant to the presence of Fe energy level results in decreasing of the energy gap for electron transition (Kong et al., 2021) and the synergism of rGO and nZVI (Fan et al., 2022), indicating that the introduction of rGO and nZVI play a critical role in improving the absorption capacity of visible light. However, in general, the narrower E_g is, the faster recombination of photo-generated charge carriers is, while 10% IGCN was not affected during, which will be discussed below.

To further explore the photoelectric conversion capability and carrier separation efficiency, transient photocurrent response and electrochemical impedance spectroscopy (EIS) are performed, as shown in Figure 6A. The smaller the radius

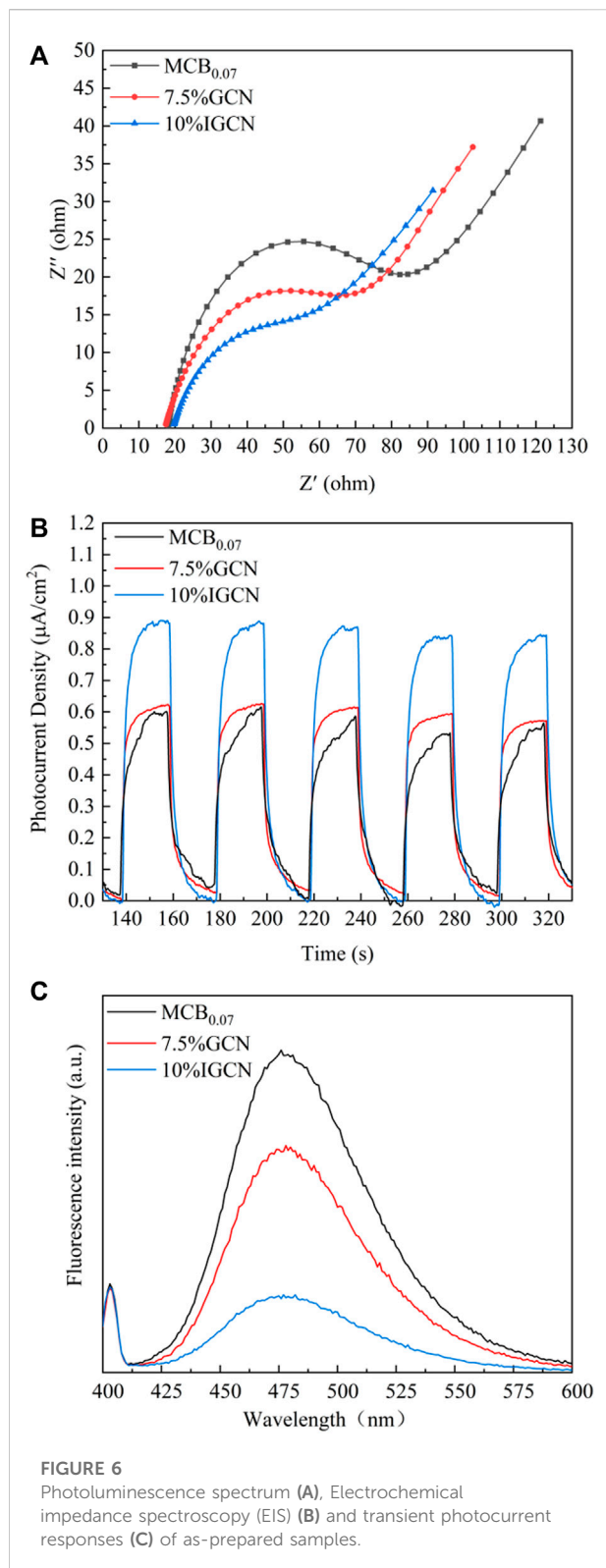


FIGURE 6
Photoluminescence spectrum (A), Electrochemical impedance spectroscopy (EIS) (B) and transient photocurrent responses (C) of as-prepared samples.

of the curve is, the lower the charge transfer resistance is. The radius of the curve for $MCB_{0.07}$ was the largest and significantly larger than 7.5% GCN, indicating that the introduction of rGO

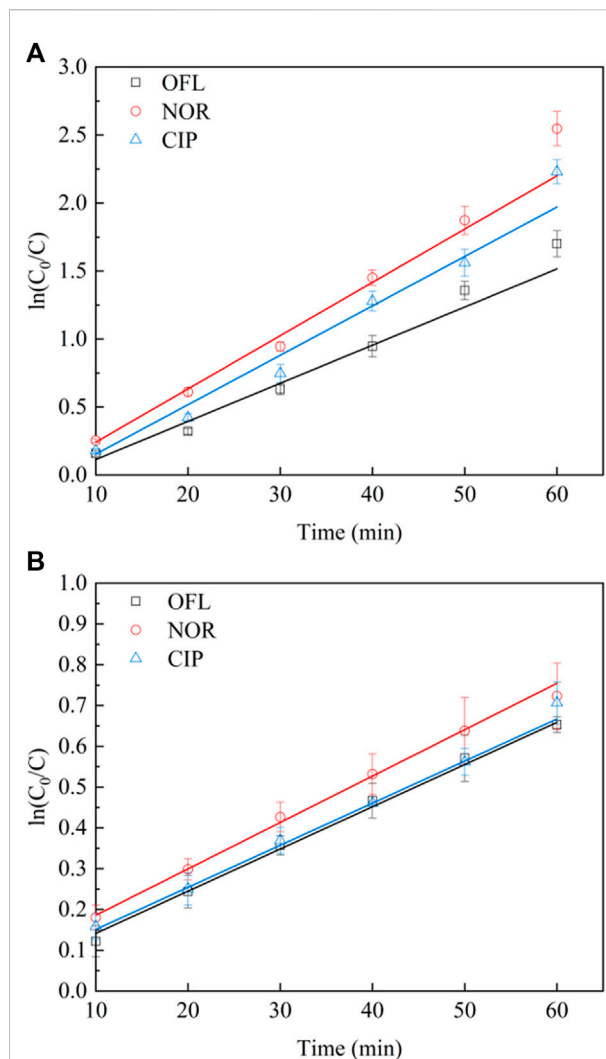


FIGURE 7
The removal efficiency of (A) antibiotic and (B) DOC on 10% IGCN.

accelerated the rate of charge transfer at the interface of the photocatalysts and reduced the charge transfer resistance of $g-C_3N_4$ (Jo et al., 2018), which could be attributed to the high charge-carrier mobility capability of the rGO sheets (Tong et al., 2015; Chen et al., 2017). With loading nZVI on 7.5% GCN, the curve radius of 10% IGCN reduced further due to the excellent conductivity of nZVI (Kong et al., 2021). Figure 6B shows that the transient photocurrent responses are recorded by switching the visible-light-on-off for five cycles. In general, the larger the photocurrent density is, the higher the photo-generated carrier mobility is. Obviously, the photocurrent density of 10% IGCN was significantly larger than that of $MCB_{0.07}$ and 7.5% GCN, which meant that 10% IGCN had good separation efficiency of photo-induced $e^- - h^+$ pairs. Similarly, the photoluminescence (PL) spectrum result also confirms that 10% IGCN possesses a

TABLE 2 Photocatalytic degradation rate constants and DOC removal rate constants of 10% IGCN during OFL, NOR, and CIP degradation.

k (min ⁻¹)	OFL		NOR		CIP	
	k	R ²	k	R ²	k	R ²
Antibiotic degradation rate constant	0.0318	0.9863	0.0450	0.9857	0.0406	0.9777
DOC removal rate constant	0.0107	0.9965	0.0110	0.9959	0.0108	0.9952

better photo-generated e⁻-h⁺ separation efficiency (Figure 6C) due to the gradually decreasing fluorescence intensity.

Notably, the narrower E_g of 10% IGCN was prone to induce photo-generated e⁻-h⁺ recombination, but the synergy between g-C₃N₄, rGO, and nZVI could effectively improve the transfer and separation efficiency of e⁻-h⁺ (Wang et al., 2019) and offset the negative effect of narrow E_g, combined with the EIS, transient photocurrent response and PL spectrum results. In addition, although Fe⁰ was oxidized due to inevitable oxidation, ≡Fe^{II} and ≡Fe^{III} on the surface of material could capture e⁻ and reduced to Fe⁰, which could improve the e⁻-h⁺ separation.

3.3 Photocatalytic performance of fluoroquinolone antibiotics

Under the visible light radiation ($\lambda > 400$ nm), the photocatalytic degradation of OFL, NOR, and CIP on 10% IGCN with time is displayed in Figure 7. The results showed that the degradation process of OFL, NOR, and CIP by 10% IGCN conforms to the first-order reaction rate equation (Table 2). The degradation rate of NOR is 0.045 min⁻¹, which is higher than that of CIP ($k = 0.0406$ min⁻¹) and OFL ($k = 0.0318$ min⁻¹). Moreover, all three antibiotics had a more significant degradation rate. The difference in degradation rate may be related to the molecular structure and the molecular weight (Fang et al., 2021).

To evaluate the mineralization of antibiotics on 10% IGCN, the change of DOC reaction rate constants in the solution was measured. As Figure 7B shows, the reaction rate constants of DOC for OFL, NOR, and CIP degradation by 10% IGCN were 0.0107 min⁻¹, 0.011 min⁻¹, and 0.0108 min⁻¹, respectively. The reaction rate constants of DOC for the three antibiotics were not significantly different. Compared with the apparent degradation effects of OFL, NOR, and CIP in Figure 7A, the DOC results showed that all three antibiotics had degradation products. However, the oxazinyl in the OFL structure is not easy to break and open (Tian et al., 2020; Zhao et al., 2021), and the cyclopropyl in the CIP structure is not easy to fall off, either (Wang et al., 2018; Bai et al., 2020; Chen et al., 2020a). These molecular structures may have a specific impact on the mineralization of antibiotics.

3.4 Possible photocatalytic mechanism

To clarify the impacts of reactive species on the photocatalytic degradation of OFL, NOR, and CIP by 10% IGCN, isopropanol (IPA), L-histidine (L-His), 1,4-benzoquinone (BQ), EDTA-2Na, and catalase was introduced to the reaction system to trap •OH, ¹O₂, •O₂⁻, h⁺, and H₂O₂.

As shown in Supplementary Figure S14 and Supplementary Table S6, after adding EDTA-2Na, the degradation kinetics of OFL, NOR, and CIP decreased to 0.0048, 0.0072, and 0.0086 min⁻¹, respectively, indicating that h⁺ played a dominant role during the photocatalytic degradation of the three antibiotics. However, from the perspective of inhibition rate (Supplementary Figure S15), compared with h⁺, the contributions of individual reactive oxygen species (ROS) (•OH, ¹O₂, •O₂⁻, and H₂O₂) do not show dramatic differences in the degradation of OFL, NOR, and CIP. In detail, the ROS inhibition rate of OFL, NOR, and CIP followed the orders: •OH (37.78%) > •O₂⁻ (32.05%) > H₂O₂ (30.79%) > ¹O₂ (23.84%), •OH (30.22%) > ¹O₂ (24.72%) > H₂O₂ (17.40%) > •O₂⁻ (16.79%), and •O₂⁻ (27.90%) > ¹O₂ (19.57%) > H₂O₂ (15.87%) > •OH (13.86%). It may be explained that the differences in the molecular structures of the antibiotics may cause the different interactions between them and the ROS (Zheng et al., 2016). Furthermore, although the scavengers quenched the target ROS, it affected the formation of other ROS through the free radical chain reaction.

Furthermore, the energy band structure of 10% IGCN was proposed to illustrate the possible photocatalytic degradation mechanism accounting for the enhancing in degradation efficiency and the complicated oxidation process. The E_g of g-C₃N₄ was obtained at 2.70 eV from the UV-Vis DRS results (Supplementary Figure S12B). The conduction band (CB) and valence band (VB) edge potentials of g-C₃N₄ can be estimated according to Supplementary Eqs S4, S6. Combined with XPS valence band spectra (Supplementary Figure S13), the calculated E_{CB} and E_{VB} of g-C₃N₄ are -1.12 eV and 1.58 eV, respectively, consistent with previous research (Chang et al., 2019).

Combined with Supplementary Table S7, the possible mechanism is proposed to explain the transformation of photo-induced charge carriers in the photocatalytic system of 10% IGCN. Under the visible light irradiation, the e⁻ of g-C₃N₄ could be promoted to the CB, leaving h⁺ in the VB. However, it should be noted that the VB of g-C₃N₄ (+1.58 eV) was higher than the redox potential of •OH/H₂O (+2.32 eV) as well as •OH/OH⁻ (+1.99 eV),

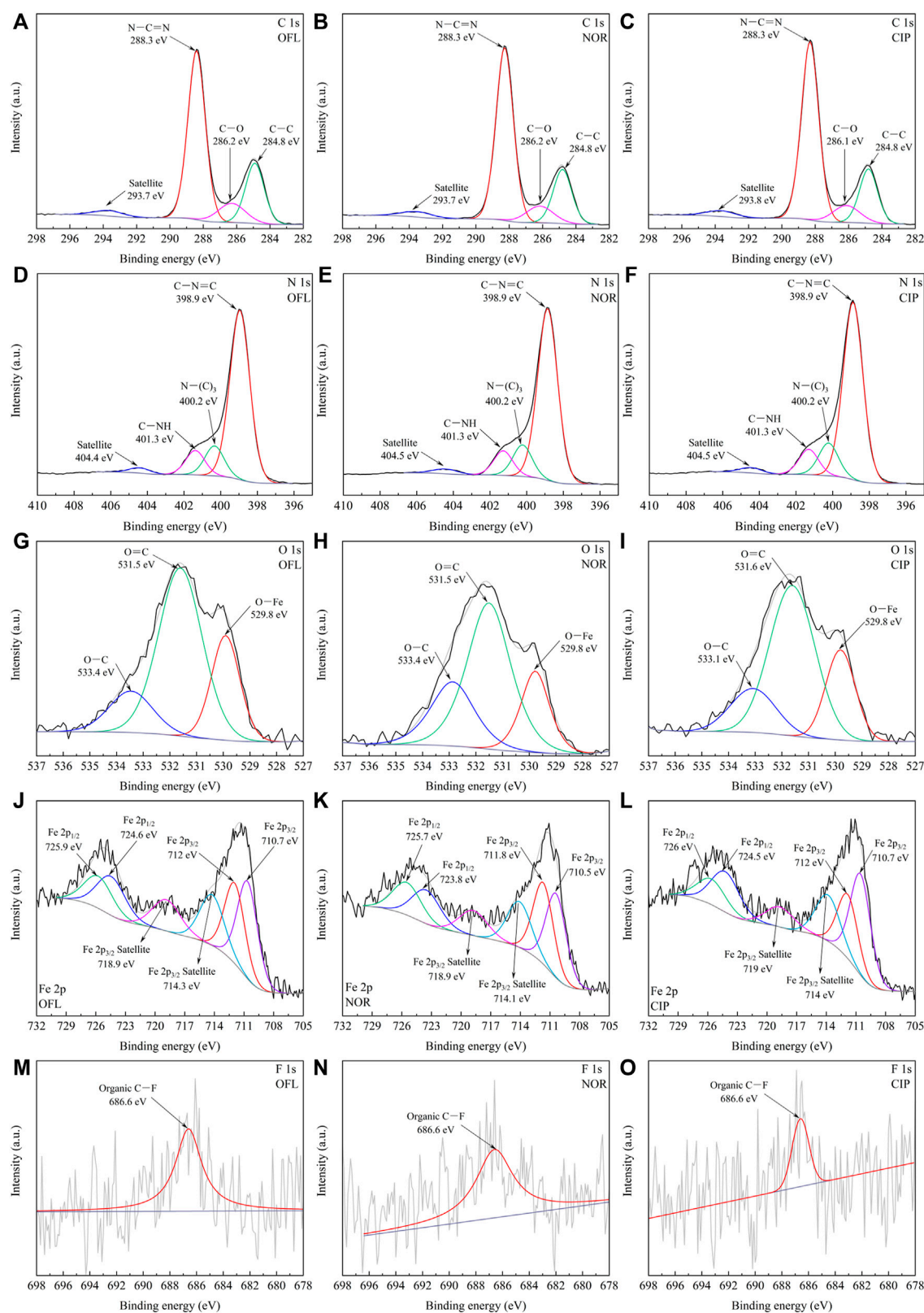


FIGURE 8

XPS spectra of 10% IGCN after the reaction, (A–C) C 1s, (D–F) N 1s, (G–I) O 1s, (J–L) Fe 2p, and (M–O) F 1s.

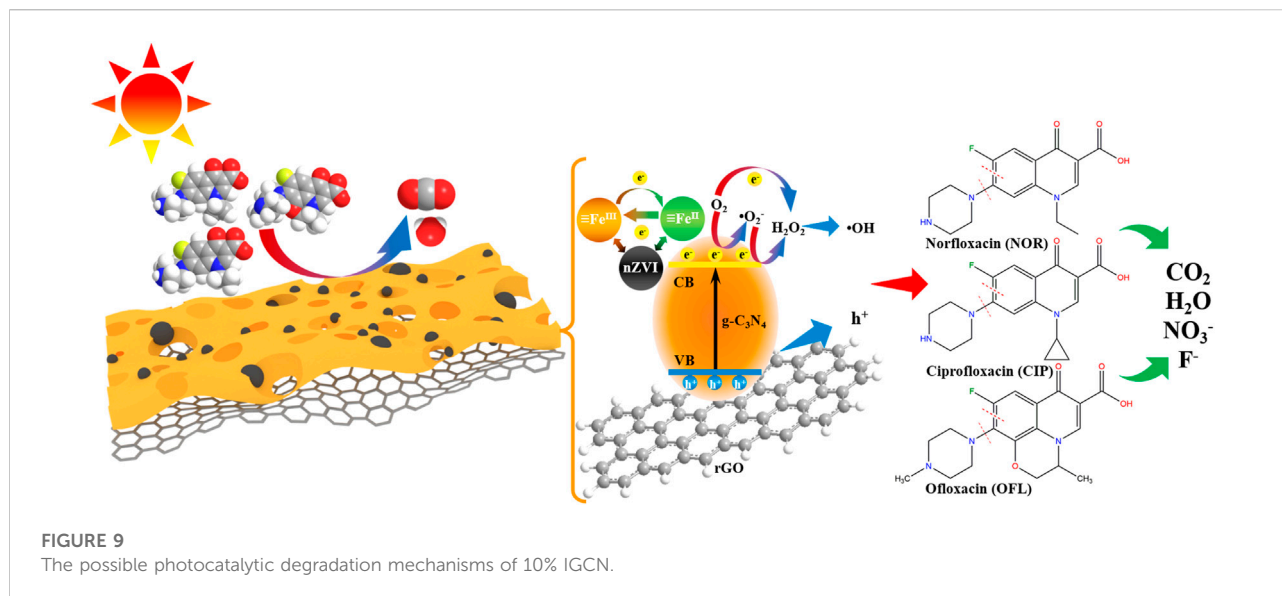


TABLE 3 The F^- concentration of OFL, NOR, and CIP in the solution before and after the reaction.

F^- concentration	CIP	NOR	OFL
Before reaction (mg/L)	0.0247	0.0157	0.0179
After reaction (mg/L)	0.1228	0.0739	0.0483
Generated (mg/L)	0.0981	0.0582	0.0303

leading to the insufficient oxidation capacity of h^+ to generate $\bullet OH$, resulting in only being produced through the free radical chain reaction. Therefore, it provided evidence that the direct oxidation of pollutants induced by h^+ , existing on the surface of the photocatalyst, was the main step in the degradation of OFL, NOR, and CIP. Furthermore, the h^+ was considered the starting point of the chain reaction, which was the source and necessary factor for producing the ROS (Zheng et al., 2019). As excellent electron mediators, e^- could be transferred from CB of $g-C_3N_4$ to rGO and then to nZVI, which meant that more e^- would be involved in the photocatalytic reaction. Moreover, owing to the interfacial interactions and synergistic effect between $g-C_3N_4$, rGO, and nZVI (Wang et al., 2019), the recombination of e^- and h^+ was largely inhibited, and the utilization of visible light was greatly improved, while the photocatalytic performance was enhanced by the following process. The CB of $g-C_3N_4$ (-1.12 eV) was lower than the redox potential of $O_2/\bullet O_2^-$ (-0.33 eV), resulting in the capability to generate $\bullet O_2^-$, which could be further oxidized into 1O_2 by h^+ ($^1O_2/\bullet O_2^-$ ($+0.65$ eV)), as well as reduced into H_2O_2 by e^- ($\bullet O_2^-/H_2O_2$ ($+0.89$ eV)). With the exception of producing the $\bullet O_2^-$, the O_2 could also capture the e^- to generate H_2O_2 (O_2/H_2O_2 ($+0.28$ eV)). As an electron trapper, H_2O_2 could be dissociated into

the $\bullet OH$ ($H_2O_2/\bullet OH$ ($+0.38$ eV)) using e^- , which may be an important source of $\bullet OH$. Although $\equiv Fe^{II}$ or $\equiv Fe^{III}$ could trap e^- to some extent to inhibit the oxidation of nZVI (Raha and Ahmaruzzaman, 2020), the nZVI is inevitably oxidized into Fe_2O_3 after the reaction (Supplementary Figure S20), attributing to the strong oxidation of ROS and activity of nZVI (Kong et al., 2021).

XPS was used to study the residues of OFL, NOR, and CIP on the surface of 10% IGCN before and after photocatalytic reaction to deduce the possible degradation intermediates. As shown in Figure 8; Supplementary Figures S16, S17, there are indistinct differences in C 1s, N 1s, and O 1s spectra. In contrast, although the Fe 2p spectra show the disappearance of the characteristic peaks of nZVI, it is speculated that the oxidation on the surface of nZVI led to no detection. However, the F 1s spectra showed a considerable change before and after the reaction (from 688.8 eV to 686.6 eV), indicating that the benzene ring attached to the C–F bond occurred as the ring-opening oxidation.

In summary, the possible photocatalytic degradation mechanisms of 10% IGCN in OFL, NOR, and CIP under visible light are proposed in Figure 9. As the main reactive species in the reaction, the h^+ may attack the C–N bond between the piperazine ring and benzene binding at first (Fan et al., 2020; Hu et al., 2020; Hu et al., 2020; Su et al., 2022), according to the DFT calculation. Moreover, the cleavage on the piperazine ring induced by h^+ was considered one of the degradation pathways because the two N atoms on the piperazine ring were also the most active sites (Hu et al., 2020; Zhang et al., 2020; Zhao et al., 2021). And then, the products could be further oxidized by $\bullet OH$ and $\bullet O_2^-$, etc. Moreover, the ring-opening oxidation of the benzene ring (C=C bond) connected by the C–F bond may also be an important step. With the exception of the above conclusion, the

defluorination is observed definitely because of the increasing concentration of F^- in OFL, NOR, and CIP solution after the photocatalytic reactions (Table 3). $\bullet OH$ and $\bullet O_2^-$ were important ROS in the defluorination process, but their mechanisms differed. Combined with the contribution of ROS, it is speculated that the fluorine was substituted by $\bullet OH$ directly in the defluorination of OFL and NOR (Jin et al., 2019; Liu et al., 2020; Zhang et al., 2020; Wang et al., 2021a). However, the defluorination process in CIP solution may be triggered by $\bullet O_2^-$ (Wang et al., 2018), which subsequently underwent $\bullet OH$ substitution, leading to the formation of the defluorination product. It can be seen that the OFL, NOR, and CIP molecules were gradually decomposed by h^+ and ROS and finally mineralized.

3.5 Recyclability and stability of photocatalysts

The stability performance of 10% IGCN photocatalyst is tested through the repeating experiment for OFL, NOR, and CIP degradation under the visible light irradiation, shown in Supplementary Figure S18. After four cycles, the removal efficiency of OFL, NOR, and CIP had a decrease from 82.71% to 71.92%, from 91.70% to 82.36%, and from 88.94% to 79.16%, respectively at 60 min, indicating the photo stability of the catalyst. The XRD patterns of the initial and used 10% IGCN composite for OFL, NOR, and CIP degradation were also conducted to further testify the stability of photocatalyst. As illustrated in Supplementary Figure S19, the diffraction peaks of nZVI are weakened, and the new peaks are consistent with Fe_2O_3 (ICDD. No. 39-0238), indicating that nZVI should be surface oxidation rather than complete oxidation, which is mutually explained with XPS results. However, the photocatalytic performance of 10% IGCN did not decrease significantly, which may be due to the existence of heterojunction between Fe_2O_3 and $g-C_3N_4$ (Shanavas et al., 2019).

4 Conclusion

In summary, a new visible-light-responsive 10% IGCN photocatalyst was prepared *via* co-modifying by nZVI and rGO on $g-C_3N_4$. It shows an improved photocatalytic performance on the degradation of antibiotics due to the enhanced visible light harvest and photogenerated charge separation. The 10% IGCN exhibited excellent photocatalytic performance for the degradation of OFL, NOR, and CIP under the irradiation of $\lambda > 400$ nm, with reaction rate constants, were 0.0318 min^{-1} , 0.045 min^{-1} , and 0.0406 min^{-1} , respectively. According to the quenching experiments, h^+ was identified as the main reactive species and played a crucial role in producing ROS. At the beginning of the reaction, h^+ could directly attack the piperazine ring or C–N bond (between the piperazine ring and benzene). The ring-opening oxidation of the benzene ring (C=C bond) linked by the C–F bond was also a vital oxidation process of

OFL, NOR, and CIP. In addition, the ROS-mediated defluorination reaction was also observed. After four cycles, the 10% IGCN maintained good photocatalytic performance and demonstrated promising potential for recycling. This work provides a new strategy to improve the photocatalytic performance of $g-C_3N_4$ by loading nZVI and rGO, and the mechanism study sheds light on the practical application of 10% IGCN on the degradation of fluoroquinolone antibiotics.

Data availability statement

The raw data supporting the conclusion of this article will be made available by the authors, without undue reservation.

Author contributions

CL: Conceptualization, data curation, formal analysis, investigation, methodology, writing—original draft. YX: Data curation, investigation, methodology. YJ: Data curation, investigation. YD: Data curation. QZ: Writing—review and editing. YS: Project administration, supervision, writing—review and editing.

Funding

This research work was supported by the National Key R&D Program of China (2022YFE0104900); the National Natural Science Foundation of China (22278007).

Conflict of interest

The authors declare that the research was conducted in the absence of any commercial or financial relationships that could be construed as a potential conflict of interest.

Publisher's note

All claims expressed in this article are solely those of the authors and do not necessarily represent those of their affiliated organizations, or those of the publisher, the editors and the reviewers. Any product that may be evaluated in this article, or claim that may be made by its manufacturer, is not guaranteed or endorsed by the publisher.

Supplementary material

The Supplementary Material for this article can be found online at: <https://www.frontiersin.org/articles/10.3389/fenvs.2022.1065770/full#supplementary-material>

References

- Adeleye, A. S., Xue, J., Zhao, Y., Taylor, A. A., Zenobio, J. E., Sun, Y., et al. (2022). Abundance, fate, and effects of pharmaceuticals and personal care products in aquatic environments. *J. Hazard. Mat.* 424, 127284. doi:10.1016/j.jhazmat.2021.127284
- Agarwal, V., and Zetterlund, P. B. (2021). Strategies for reduction of graphene oxide – a comprehensive review. *Chem. Eng. J.* 405, 127018. doi:10.1016/j.cej.2020.127018
- Bai, F., Ni, S., Tang, Y., Pan, X., and Zhao, Z. (2020). Ciprofloxacin transformation in aqueous environments: Mechanism, kinetics, and toxicity assessment during •OH-mediated oxidation. *Sci. Total Environ.* 699, 134190. doi:10.1016/j.scitotenv.2019.134190
- Balakrishnan, A., and Chinthala, M. (2022). Comprehensive review on advanced reusability of g-C₃N₄ based photocatalysts for the removal of organic pollutants. *Chemosphere* 297, 134190. doi:10.1016/j.chemosphere.2022.134190
- Chang, X., Yao, X., Ding, N., Yin, X., Zheng, Q., Lu, S., et al. (2019). Photocatalytic degradation of trihalomethanes and haloacetonitriles on graphitic carbon nitride under visible light irradiation. *Sci. Total Environ.* 682, 200–207. doi:10.1016/j.scitotenv.2019.05.075
- Chen, F., An, W., Liu, L., Liang, Y., and Cui, W. (2017). Highly efficient removal of bisphenol A by a three-dimensional graphene hydrogel-AgBr@rGO exhibiting adsorption/photocatalysis synergy. *Appl. Catal. B Environ.* 217, 65–80. doi:10.1016/j.apcatb.2017.05.078
- Chen, F., Liu, L., Chen, J., Li, W., Chen, Y., Zhang, Y., et al. (2021). Efficient decontamination of organic pollutants under high salinity conditions by a nonradical peroxymonosulfate activation system. *Water Res.* 191, 116799. doi:10.1016/j.watres.2020.116799
- Chen, L., Ni, R., Yuan, T., Gao, Y., Kong, W., Zhang, P., et al. (2020a). Effects of green synthesis, magnetization, and regeneration on ciprofloxacin removal by bimetallic nZVI/Cu composites and insights of degradation mechanism. *J. Hazard. Mat.* 382, 121008. doi:10.1016/j.jhazmat.2019.121008
- Chen, T., Zhang, J., Ge, H., Li, M., Li, Y., Liu, B., et al. (2020b). Efficient extraction of uranium in organics-containing wastewater over g-C₃N₄/GO hybrid nanosheets with type-II band structure. *J. Hazard. Mat.* 384, 121383. doi:10.1016/j.jhazmat.2019.121383
- Cui, Y., An, X., Zhang, S., Tang, Q., Lan, H., Liu, H., et al. (2021). Emerging graphitic carbon nitride-based membranes for water purification. *Water Res.* 200, 117207. doi:10.1016/j.watres.2021.117207
- Fan, M., Zhang, P., Wang, C., Tang, J., and Sun, H. (2022). Tailored design of three-dimensional rGOA-nZVI catalyst as an activator of persulfate for degradation of organophosphorus pesticides. *J. Hazard. Mat.* 428, 128254. doi:10.1016/j.jhazmat.2022.128254
- Fan, Y., Zhou, Z., Feng, Y., Zhou, Y., Wen, L., and Shih, K. (2020). Degradation mechanisms of ofloxacin and cefazolin using peroxymonosulfate activated by reduced graphene oxide-CoFe₂O₄ composites. *Chem. Eng. J.* 383, 123056. doi:10.1016/j.cej.2019.123056
- Fang, L., Miao, Y., Wei, D., Zhang, Y., and Zhou, Y. (2021). Efficient removal of norfloxacin in water using magnetic molecularly imprinted polymer. *Chemosphere* 262, 128032. doi:10.1016/j.chemosphere.2020.128032
- Feng, Y., Chen, G., Zhang, Y., Li, D., Ling, C., Wang, Q., et al. (2022). Superhigh co-adsorption of tetracycline and copper by the ultrathin g-C₃N₄ modified graphene oxide hydrogels. *J. Hazard. Mat.* 424, 127362. doi:10.1016/j.jhazmat.2021.127362
- He, W., Liu, L., Ma, T., Han, H., Zhu, J., Liu, Y., et al. (2022). Controllable morphology CoFe₂O₄/g-C₃N₄ p-n heterojunction photocatalysts with built-in electric field enhance photocatalytic performance. *Appl. Catal. B Environ.* 306, 121107. doi:10.1016/j.apcatb.2022.121107
- Hu, K., Li, R., Ye, C., Wang, A., Wei, W., Hu, D., et al. (2020). Facile synthesis of Z-scheme composite of TiO₂ nanorod/g-C₃N₄ nanosheet efficient for photocatalytic degradation of ciprofloxacin. *J. Clean. Prod.* 253, 120055. doi:10.1016/j.jclepro.2020.120055
- Hu, X., Hu, X., Peng, Q., Zhou, L., Tan, X., Jiang, L., et al. (2020). Mechanisms underlying the photocatalytic degradation pathway of ciprofloxacin with heterogeneous TiO₂. *Chem. Eng. J.* 380, 122366. doi:10.1016/j.cej.2019.122366
- Hu, Y., Zhou, C., Wang, H., Chen, M., Zeng, G., Liu, Z., et al. (2021). Recent advance of graphene/semiconductor composite nanocatalysts: Synthesis, mechanism, applications and perspectives. *Chem. Eng. J.* 414, 128795. doi:10.1016/j.cej.2021.128795
- Huang, C., Wen, Y., Ma, J., Dong, D., Shen, Y., Liu, S., et al. (2021). Unraveling fundamental active units in carbon nitride for photocatalytic oxidation reactions. *Nat. Commun.* 12 (1), 320. doi:10.1038/s41467-020-20521-5
- Huang, X., Zhang, F., Peng, K., Liu, J., Lu, L., and Li, S. (2020). Effect and mechanism of graphene structured palladized zero-valent iron nanocomposite (nZVI-Pd/NG) for water denitration. *Sci. Rep.* 10 (1), 9931. doi:10.1038/s41598-020-66725-z
- Jaiswal, A., Pal, S., Kumar, A., and Prakash, R. (2020). Metal free triad from red phosphorous, reduced graphene oxide and graphitic carbon nitride (red P-rGO-g-C₃N₄) as robust electro-catalysts for hydrogen evolution reaction. *Electrochimica Acta* 338, 135851. doi:10.1016/j.electacta.2020.135851
- Jin, X., Zhou, X., Sun, P., Lin, S., Cao, W., Li, Z., et al. (2019). Photocatalytic degradation of norfloxacin using N-doped TiO₂: Optimization, mechanism, identification of intermediates and toxicity evaluation. *Chemosphere* 237, 124433. doi:10.1016/j.chemosphere.2019.124433
- Jo, W., Kumar, S., Eslava, S., and Tonda, S. (2018). Construction of Bi₂WO₆/RGO/g-C₃N₄ 2D/2D/2D hybrid Z-scheme heterojunctions with large interfacial contact area for efficient charge separation and high-performance photoreduction of CO₂ and H₂O into solar fuels. *Appl. Catal. B Environ.* 239, 586–598. doi:10.1016/j.apcatb.2018.08.056
- Kasinathan, M., Thiripuranthagan, S., and Sivakumar, A. (2020). A facile fabrication of Br-modified g-C₃N₄/rGO composite catalyst for enhanced visible photocatalytic activity towards the degradation of harmful dyes. *Mat. Res. Bull.* 130, 110870. doi:10.1016/j.materresbull.2020.110870
- Kim, J., Kim, H., Choi, J., and Baek, K. (2020). Bifunctional iron-modified graphitic carbon nitride (g-C₃N₄) for simultaneous oxidation and adsorption of arsenic. *Environ. Res.* 188, 109832. doi:10.1016/j.envres.2020.109832
- Kong, W., Yue, Q., Gao, Y., Li, Q., Xu, X., Kong, Y., et al. (2021). Enhanced photodegradation of sulfadiazine via PAA/g-C₃N₄-Fe⁰ polymeric catalysts under visible light. *Chem. Eng. J.* 413, 127456. doi:10.1016/j.cej.2020.127456
- Li, Y., Wang, J., Yang, Y., Zhang, Y., He, D., An, Q., et al. (2015). Seed-induced growing various TiO₂ nanostructures on g-C₃N₄ nanosheets with much enhanced photocatalytic activity under visible light. *J. Hazard. Mat.* 292, 79–89. doi:10.1016/j.jhazmat.2015.03.006
- Liang, Z., Wen, Q., Wang, X., Zhang, F., and Yu, Y. (2016). Chemically stable and reusable nano zero-valent iron/graphite-like carbon nitride nanohybrid for efficient photocatalytic treatment of Cr(VI) and rhodamine B under visible light. *Appl. Surf. Sci.* 386, 451–459. doi:10.1016/j.apsusc.2016.06.010
- Lin, J., Tian, W., Zhang, H., Duan, X., Sun, H., Wang, H., et al. (2022). Carbon nitride-based Z-scheme heterojunctions for solar-driven advanced oxidation processes. *J. Hazard. Mat.* 434, 128866. doi:10.1016/j.jhazmat.2022.128866
- Liu, W., Li, Y., Liu, F., Jiang, W., Zhang, D., and Liang, J. (2019). Visible-light-driven photocatalytic degradation of diclofenac by carbon quantum dots modified porous g-C₃N₄: Mechanisms, degradation pathway and DFT calculation. *Water Res.* 151, 8–19. doi:10.1016/j.watres.2018.11.084
- Liu, W., Zhou, J., and Yao, J. (2020). Shuttle-like CeO₂/g-C₃N₄ composite combined with persulfate for the enhanced photocatalytic degradation of norfloxacin under visible light. *Ecotoxicol. Environ. Saf.* 190, 110062. doi:10.1016/j.ecoenv.2019.110062
- Liu, Y., Jin, W., Zhao, Y., Zhang, G., and Zhang, W. (2017). Enhanced catalytic degradation of methylene blue by α-Fe₂O₃/graphene oxide via heterogeneous photo-Fenton reactions. *Appl. Catal. B Environ.* 206, 642–652. doi:10.1016/j.apcatb.2017.01.075
- Lu, J., Ji, Y., Chovelon, J., and Lu, J. (2021). Fluoroquinolone antibiotics sensitized photodegradation of isoproturon. *Water Res.* 198, 117136. doi:10.1016/j.watres.2021.117136
- Lv, H., Niu, H., Zhao, X., Cai, Y., and Wu, F. (2021). Carbon zero-valent iron materials possessing high-content fine Fe⁰ nanoparticles with enhanced microelectrolysis-Fenton-like catalytic performance for water purification. *Appl. Catal. B Environ.* 286, 119940. doi:10.1016/j.apcatb.2021.119940
- Ma, Y., Lv, X., Xiong, D., Zhao, X., and Zhang, Z. (2021). Catalytic degradation of ranitidine using novel magnetic Ti₃C₂-based MXene nanosheets modified with nanoscale zero-valent iron particles. *Appl. Catal. B Environ.* 284, 119720. doi:10.1016/j.apcatb.2020.119720
- Mangla, D., Annu, Sharma, A., and Ikram, S. (2022). Critical review on adsorptive removal of antibiotics: Present situation, challenges and future perspective. *J. Hazard. Mat.* 425, 127946. doi:10.1016/j.jhazmat.2021.127946
- Nemiwal, M., Zhang, T. C., and Kumar, D. (2021). Recent progress in g-C₃N₄, TiO₂ and ZnO based photocatalysts for dye degradation: Strategies to improve photocatalytic activity. *Sci. Total Environ.* 767, 144896. doi:10.1016/j.scitotenv.2020.144896
- Oberoi, A. S., Jia, Y., Zhang, H., Khanal, S. K., and Lu, H. (2019). Insights into the fate and removal of antibiotics in engineered biological treatment systems: A critical review. *Environ. Sci. Technol.* 53 (13), 7234–7264. doi:10.1021/acs.est.9b01131
- Ong, W., Tan, L., Ng, Y. H., Yong, S., and Chai, S. (2016). Graphitic carbon nitride (g-C₃N₄)-based photocatalysts for artificial photosynthesis and environmental remediation: Are we a step closer to achieving sustainability? *Chem. Rev.* 116 (12), 7159–7329. doi:10.1021/acs.chemrev.6b00075

- Palanivel, B., Lallimathi, M., Arjunker, B., Shkir, M., Alshahrani, T., Al-Namshah, K. S., et al. (2021). rGO supported g-C₃N₄/CoFe₂O₄ heterojunction: Visible-light-active photocatalyst for effective utilization of H₂O₂ to organic pollutant degradation and OH radicals production. *J. Environ. Chem. Eng.* 9 (1), 104698. doi:10.1016/j.jece.2020.104698
- Raha, S., and Ahmaruzzaman, M. (2020). Enhanced performance of a novel superparamagnetic g-C₃N₄/NiO/ZnO/Fe₃O₄ nanohybrid photocatalyst for removal of esomeprazole: Effects of reaction parameters, co-existing substances and water matrices. *Chem. Eng. J.* 395, 124969. doi:10.1016/j.cej.2020.124969
- Rao, Z., Zhu, N., Wei, X., Li, F., Wu, P., Dang, Z., et al. (2021). Efficient peroxydisulfate activation with nZVI/CuO@BC nanocomposite derived from wastes for degradation of tetrabromobisphenol A in alkaline environment. *J. Hazard. Mat.* 417, 126029. doi:10.1016/j.jhazmat.2021.126029
- Saha, D., Visconti, M. C., Desipio, M. M., and Thorpe, R. (2020). Inactivation of antibiotic resistance gene by ternary nanocomposites of carbon nitride, reduced graphene oxide and iron oxide under visible light. *Chem. Eng. J.* 382, 122857. doi:10.1016/j.cej.2019.122857
- Saya, L., Malik, V., Gautam, D., Gambhir, G., BalendraSingh, W. R., Hooda, S., et al. (2022). A comprehensive review on recent advances toward sequestration of levofloxacin antibiotic from wastewater. *Sci. Total Environ.* 813, 152529. doi:10.1016/j.scitotenv.2021.152529
- Schnabel, T., Jautz, N., Mehling, S., Springer, C., and Londong, J. (2021). Photocatalytic degradation of hydrocarbons and methylene blue using floatable titanium dioxide catalysts in contaminated water. *Water Reuse* 11 (2), 224–235. doi:10.2166/wrd.2021.118
- Shanavas, S., Mohana Roopan, S., Priyadharsan, A., Devipriya, D., Jayapandi, S., Acevedo, R., et al. (2019). Computationally guided synthesis of (2D/3D/2D) rGO/Fe₂O₃/g-C₃N₄ nanostructure with improved charge separation and transportation efficiency for degradation of pharmaceutical molecules. *Appl. Catal. B Environ.* 255, 117758. doi:10.1016/j.apcatb.2019.117758
- Shao, L., Jiang, D., Xiao, P., Zhu, L., Meng, S., and Chen, M. (2016). Enhancement of g-C₃N₄ nanosheets photocatalysis by synergistic interaction of ZnS microsphere and RGO inducing multistep charge transfer. *Appl. Catal. B Environ.* 198, 200–210. doi:10.1016/j.apcatb.2016.05.056
- Su, Q., Li, J., Yuan, H., Wang, B., Wang, Y., Li, Y., et al. (2022). Visible-light-driven photocatalytic degradation of ofloxacin by g-C₃N₄/NH₂-MLL-88B(Fe) heterostructure: Mechanisms, DFT calculation, degradation pathway and toxicity evolution. *Chem. Eng. J.* 427, 131594. doi:10.1016/j.cej.2021.131594
- Tang, Z., He, W., Wang, Y., Wei, Y., Yu, X., Xiong, J., et al. (2022). Ternary heterojunction in rGO-coated Ag/Cu₂O catalysts for boosting selective photocatalytic CO₂ reduction into CH₄. *Appl. Catal. B Environ.* 311, 121371. doi:10.1016/j.apcatb.2022.121371
- Tian, Y., He, X., Chen, W., Tian, X., Nie, Y., Han, B., et al. (2020). Significant enhancement of photo-Fenton degradation of ofloxacin over Fe-Dis@Sep due to highly dispersed FeC₆ with electron deficiency. *Sci. Total Environ.* 723, 138144. doi:10.1016/j.scitotenv.2020.138144
- Tong, Z., Yang, D., Shi, J., Nan, Y., Sun, Y., and Jiang, Z. (2015). Three-Dimensional porous aerogel constructed by g-C₃N₄ and graphene oxide nanosheets with excellent visible-light photocatalytic performance. *ACS Appl. Mat. Interfaces* 7 (46), 25693–25701. doi:10.1021/acsami.5b09503
- Wallmann, L., Krampe, J., Lahnsteiner, J., Radu, E., van Rensburg, P., Slipko, K., et al. (2021). Fate and persistence of antibiotic-resistant bacteria and genes through a multi-barrier treatment facility for direct potable reuse. *Water Reuse* 11 (3), 373–390. doi:10.2166/wrd.2021.097
- Wang, F., Feng, Y., Chen, P., Wang, Y., Su, Y., Zhang, Q., et al. (2018). Photocatalytic degradation of fluoroquinolone antibiotics using ordered mesoporous g-C₃N₄ under simulated sunlight irradiation: Kinetics, mechanism, and antibacterial activity elimination. *Appl. Catal. B Environ.* 227, 114–122. doi:10.1016/j.apcatb.2018.01.024
- Wang, M., Yu, H., Wang, P., Chi, Z., Zhang, Z., Dong, B., et al. (2021a). Promoted photocatalytic degradation and detoxification performance for norfloxacin on Z-scheme phosphate-doped BiVO₄/graphene quantum dots/P-doped g-C₃N₄. *Sep. Purif. Technol.* 274, 118692. doi:10.1016/j.seppur.2021.118692
- Wang, X., Hong, M., Zhang, F., Zhuang, Z., and Yu, Y. (2016). Recyclable nanoscale zero valent iron doped g-C₃N₄/MoS₂ for efficient photocatalysis of RhB and Cr(VI) driven by visible light. *ACS Sustain. Chem. Eng.* 4 (7), 4055–4063. doi:10.1021/acsuschemeng.6b01024
- Wang, X., Lu, M., Ma, J., and Ning, P. (2019). Preparation of air-stable magnetic g-C₃N₄@FeO-graphene composite by new reduction method for simultaneous and synergistic conversion of organic dyes and heavy metal ions in aqueous solution. *Sep. Purif. Technol.* 212, 586–596. doi:10.1016/j.seppur.2018.11.052
- Wang, X., Pu, X., Yuan, Y., Xiang, Y., Zhang, Y., Xiong, Z., et al. (2020). An old story with new insight into the structural transformation and radical production of micron-scale zero-valent iron on successive reactivities. *Chin. Chem. Lett.* 31 (10), 2634–2640. doi:10.1016/j.ccl.2020.08.007
- Wang, X., Wang, Y., Ma, J., and Ning, P. (2022). Band gap narrowing ternary phosphorus-doped g-C₃N₄/FeO@expanded graphite carbon layer hybrid composite for effective degradation of tetracycline via multiply synergistic mechanisms. *J. Environ. Chem. Eng.* 10 (3), 107589. doi:10.1016/j.jece.2022.107589
- Wang, X., Zhou, Z., Liang, Z., Zhuang, Z., and Yu, Y. (2017). Photochemical synthesis of the Fe⁰/C₃N₄/MoS₂ heterostructure as a highly active and reusable photocatalyst. *Appl. Surf. Sci.* 423, 225–235. doi:10.1016/j.apsusc.2017.06.050
- Wang, Y., Zhang, P., Li, T., Lyu, L., Gao, Y., and Hu, C. (2021b). Enhanced Fenton-like efficiency by the synergistic effect of oxygen vacancies and organics adsorption on FeOy-d-g-C₃N₄ with Fe–N complexation. *J. Hazard. Mat.* 408, 124818. doi:10.1016/j.jhazmat.2020.124818
- Wu, X., Wang, X., Xie, Y., Ren, N., Ma, J., and Ning, P. (2022a). Facile *in-situ* construction of highly dispersed nano zero-valent iron modified black TiO₂ Z-scheme recyclable heterojunction with highly efficient visible-light-driven photocatalytic activity. *Appl. Catal. B Environ.* 310, 121325. doi:10.1016/j.apcatb.2022.121325
- Wu, Z., Tong, Z., Xie, Y., Sun, H., Gong, X., Qin, P., et al. (2022b). Efficient degradation of tetracycline by persulfate activation with Fe, Co and O co-doped g-C₃N₄: Performance, mechanism and toxicity. *Chem. Eng. J.* 434, 134732. doi:10.1016/j.cej.2022.134732
- Xiao, J., Liu, Q., Song, M., Li, X., Li, Q., and Shang, J. K. (2021). Directing photocatalytic pathway to exceedingly high antibacterial activity in water by functionalizing holey ultrathin nanosheets of graphitic carbon nitride. *Water Res.* 198, 117125. doi:10.1016/j.watres.2021.117125
- Xie, Y., Yin, X., Jiao, Y., Sun, Y., and Wang, C. (2022). Visible-light-responsive photocatalytic inactivation of ofloxacin-resistant bacteria by rGO modified g-C₃N₄. *Environ. Sci. Pollut. Res.* 29, 63142–63154. doi:10.1007/s11356-022-20326-7
- Yuan, D., Huang, W., Chen, X., Li, Z., Ding, J., Wang, L., et al. (2019). Introduction of in-plane π-conjugated heterojunction via rGO modulation: A promising approach to enhance photoexcited charge separation and transfer of g-C₃N₄. *Appl. Surf. Sci.* 489, 658–667. doi:10.1016/j.apsusc.2019.05.303
- Zeng, Z., Fan, Y., Quan, X., Yu, H., Chen, S., and Zhang, S. (2020). Energy-transfer-mediated oxygen activation in carbonyl functionalized carbon nitride nanosheets for high-efficient photocatalytic water disinfection and organic pollutants degradation. *Water Res.* 177, 115798. doi:10.1016/j.watres.2020.115798
- Zewdie, T. M., Habtu, N. G., Dutta, A., and Van der Bruggen, B. (2021). Solar-assisted membrane technology for water purification: A review. *Water Reuse* 11 (1), 1–32. doi:10.2166/wrd.2020.049
- Zhang, D., Qi, J., Ji, H., Li, S., Chen, L., Huang, T., et al. (2020). Photocatalytic degradation of ofloxacin by perovskite-type NaNbO₃ nanorods modified g-C₃N₄ heterojunction under simulated solar light: Theoretical calculation, ofloxacin degradation pathways and toxicity evolution. *Chem. Eng. J.* 400, 125918. doi:10.1016/j.cej.2020.125918
- Zhao, G., Ding, J., Zhou, F., Chen, X., Wei, L., Gao, Q., et al. (2021). Construction of a visible-light-driven magnetic dual Z-scheme BiVO₄/g-C₃N₄/NiFe₂O₄ photocatalyst for effective removal of ofloxacin: Mechanisms and degradation pathway. *Chem. Eng. J.* 405, 126704. doi:10.1016/j.cej.2020.126704
- Zheng, D., Yin, G., Liu, M., Chen, C., Jiang, Y., Hou, L., et al. (2021). A systematic review of antibiotics and antibiotic resistance genes in estuarine and coastal environments. *Sci. Total Environ.* 777, 146009. doi:10.1016/j.scitotenv.2021.146009
- Zheng, Q., Durkin, D. P., Elenewski, J. E., Sun, Y., Banek, N. A., Hua, L., et al. (2016). Visible-light-responsive graphitic carbon nitride: Rational design and photocatalytic applications for water treatment. *Environ. Sci. Technol.* 50 (23), 12938–12948. doi:10.1021/acs.est.6b02579
- Zheng, Q., Shen, H., and Shuai, D. (2017). Emerging investigators series: Advances and challenges of graphitic carbon nitride as a visible-light-responsive photocatalyst for sustainable water purification. *Environ. Sci. Water Res. Technol.* 3 (6), 982–1001. doi:10.1039/C7EW00159B
- Zheng, Q., Xu, E., Park, E., Chen, H., and Shuai, D. (2019). Looking at the overlooked hole oxidation: Photocatalytic transformation of organic contaminants on graphitic carbon nitride under visible light irradiation. *Appl. Catal. B Environ.* 240, 262–269. doi:10.1016/j.apcatb.2018.09.012
- Zhou, C., Lai, C., Huang, D., Zeng, G., Zhang, C., Cheng, M., et al. (2018). Highly porous carbon nitride by supramolecular preassembly of monomers for photocatalytic removal of sulfamethazine under visible light driven. *Appl. Catal. B Environ.* 220, 202–210. doi:10.1016/j.apcatb.2017.08.055
- Zhou, L., Han, P., Zhao, M., Yu, Y., Sun, D., Hou, L., et al. (2021). Biotransformation of lincomycin and fluoroquinolone antibiotics by the ammonia oxidizers aoa, aob and comammox: A comparison of removal, pathways, and mechanisms. *Water Res.* 196, 117003. doi:10.1016/j.watres.2021.117003
- Zhu, L., Santiago-Schübel, B., Xiao, H., Hollert, H., and Kueppers, S. (2016). Electrochemical oxidation of fluoroquinolone antibiotics: Mechanism, residual antibacterial activity and toxicity change. *Water Res.* 102, 52–62. doi:10.1016/j.watres.2016.06.005